Research Square

Preprints are preliminary reports that have not undergone peer review.
They should not be considered conclusive, used to inform clinical practice,
or referenced by the media as validated information.

Heat stress along the 2026 Tour de France: a spatiotemporal reconstruction of exposure across race stages

Jon Xavier Olano Pozo

jonxavier.olano@urv.cat

Universitat Rovira i Virgili

Antoni Domènech-Montaña

Universitat Rovira i Virgili

Anna Boqué-Ciurana

Universitat Rovira i Virgili

Òscar Saladié-Borraz

Universitat Rovira i Virgili

Article

Keywords: cycling, Tour de France, heat stress, UTCI, WBGT, spatiotemporal exposure, climate change

Posted Date: November 6th, 2026

DOI: https://doi.org/10.21203/rs.3.rs-11319470/v1

License: This work is licensed under a Creative Commons Attribution 4.0 International License.
Read Full License

Additional Declarations: No competing interests reported.

Heat stress along the 2026 Tour de France: a spatiotemporal reconstruction of exposure across race stages

Jon Xavier Olano Pozo, Institut Universitari de Recerca en Sostenibilitat, Canvi Climàtic i Transició Energètica, Centre de Canvi Climàtic, Universitat Rovira i Virgili, Joanot Martorell 15, Vila-seca, Tarragona, Spain. **Corresponding Author: jonxavier.olano@urv.cat**

Antoni Domènech, Institut Universitari de Recerca en Sostenibilitat, Canvi Climàtic i Transició Energètica, Centre en Canvi Climàtic C3, Universitat Rovira i Virgili, Joanot Martorell 15, Vila-seca, Tarragona, Spain. antoni.domenech@urv.cat

Anna Boqué-Ciurana, Institut Universitari de Recerca en Sostenibilitat, Canvi Climàtic i Transició Energètica, Centre en Canvi Climàtic C3, Universitat Rovira i Virgili, Joanot Martorell 15, Vila-seca, Tarragona, Spain. anna.boque@urv.cat

Òscar Saladié, Department of Geography, Universitat Rovira i Virgili, Joanot Martorell 15, Vila-seca, Tarragona, Spain. oscar.saladie@urv.cat

Abstract

Anthropogenic climate change is amplifying the intensity and frequency of extreme summer heat across Europe, posing critical thermal challenges for major outdoor endurance events. However, existing sports heat protocols typically rely on static weather measurements, failing to capture the microclimatic variability encountered by a moving event. Here, we present a high-resolution spatiotemporal reconstruction of environmental heat stress across all 21 stages (~3,323 km) of the 2026 Tour de France. By integrating ERA5 reanalysis and WRF mesoscale modeling (~1 km resolution) corrected with ground station networks, modeled the Universal Thermal Climate Index (UTCI) and the Wet-Bulb Globe Temperature (WBGT) paired with estimated peloton passage times. Strong to very strong heat stress (UTCI ≥ 32 °C) accounted for 60.5% (2,009 km) of the total route distance and 57.8% (2,991 min) of estimated riding time, peaking at 44.5 °C in Stage 4. Although no segment exceeded the Union Cycliste Internationale (UCI) threshold for stage suspension (WBGT ≥ 32.2 °C), 175.9 km fell within high-risk Red band conditions (WBGT ≥ 28 °C). This index divergence reveals that while dynamic athlete movement can mitigate immediate regulatory breaches, static roadside spectators endure prolonged exposure under dangerous radiant loads. These findings underscore the need for mobile, spatiotemporally resolved biometeorological frameworks in sports safety protocols and event scheduling.

Keywords: cycling; Tour de France; heat stress; UTCI; WBGT, spatiotemporal exposure; climate change.

1. Introduction

Human-induced climate change has increased the frequency, duration, and intensity of extreme heat across Europe, with warming trends projected to exacerbate conditions during summer months(IPCC, 2021). These shifting thermal regimes affect outdoor activities, labor safety and leisure pursuits (Obradovich & Fowler, 2017; Boqué-Ciurana et al., 2025; Olano et al., 2026). Their implications extend beyond exceptionally hot days: the timing, duration, and location of an activity determine the conditions people encounter (Saladié et al., 2025). Analyses of recreational physical activity have found that acutely hot conditions can reduce participation, although responses differ by season and region (Obradovich & Fowler, 2017). In organised mass-participation and elite endurance events, participants, operational staff and spectators have little flexibility to avoid adverse conditions once competition is underway, creating complex public health and operational challenges (Racinais et al., 2015; Brocherie et al., 2015).

Heat presents a particular challenge during endurance exercise because metabolic heat production accompanies prolonged outdoor exposure. During high-intensity cycling, athletes routinely sustain internal work rates generating over 1,000–1,200 W of metabolic heat, of which roughly 75–80% must be dissipated to prevent uncompensable heat storage (Périard et al., 2021). The capacity to dissipate this thermal load relies on the environmental microclimate: air temperature, humidity, radiation, and wind influence dry and evaporative heat exchanges. When cooling mechanisms fail, core body temperature escalates toward dangerous thresholds (>38.5–39.5°C), precipitating cardiovascular strain, blunted neuromuscular recruitment, gastrointestinal barrier disruption, and, in severe cases, life-threatening exertional heat stroke (Roberts et al., 2023; Périard et al., 2021). To manage these vulnerabilities, sports medicine guidelines and the Union Cycliste Internationale (UCI) Extreme Weather Protocol rely on environmental safety indices (such as the Wet-Bulb Globe Temperature) to activate preventive cooling countermeasures, modify feed zones, or truncate race sectors (Racinais et al., 2015; Racinais et al. 2023; UCI, 2023). However, field data show that performance varies with ambient temperature, with lower maximal power observed under particularly hot conditions (Valenzuela et al., 2022). Measurements taken during a multistage professional race further demonstrate the complexity of the relationship between environmental indices, work rate, and physiological strain. Périard et al. (2023) found associations between several thermal indices and power output, but measures of riders' physiological strain did not respond the same way to every index. These findings support a careful distinction between describing environmental heat stress and estimating an individual rider's health risk.

The Tour de France provides a distinctive setting for examining environmental exposure. Over three weeks, stages traverse heterogeneous topographies ranging from wind-exposed coastal plains to deep river valleys, urban corridors, and mountain passes. In enclosed valley bottoms, subsidence, thermal inversions, and blocked wind regimes

frequently create extreme local heat traps. Compounding ambient air temperature, the asphalt surface emits substantial long-wave thermal radiation (often exceeding air temperature by 15–20 °C) directly beneath the athletes. Furthermore, not only changing terrain characteristics and weather as the day progresses influences the thermal comfort, but also the aerodynamics of cycling among the peloton, in a small group or alone conditions it. Within the dense peloton, convective cooling is markedly attenuated compared to the leading edge of the race, while localized vapor pressure builds from collective sweat evaporation. Also, during steep mountain ascents, where metabolic heat production peaks, riding speeds drop abruptly (often below 15–20 km/h), reducing convective and evaporative dissipation precisely when internal heat generation is at its maximum. However, the literature analysing this diversity of conditions is almost non-existent. Cvijanovic et al. (2026) analysed heat stress across France using 50 years of July conditions and historical Tour dates. They found an increase in July heat stress and identified locations where values have been high. Their study also highlighted a remaining challenge: observations at fixed locations and hours cannot fully represent the changing conditions encountered along a moving race route.

The exposure along the race route is not confined to the riders. Hundreds of thousands of spectators gather on the roadside for extended periods. They are predominantly static, directly exposed to open-sky solar irradiance and radiant heat from the asphalt with limited access to shade or active cooling, rendering them vulnerable to heat-related issues (Matzarakis & Fröhlich, 2015). Previous research on outdoor gatherings and public exhibitions has shown the need to match thermal conditions to the exact hours and spaces of participation (Saladié et al., 2025; Boqué-Ciurana et al., 2025). In professional cycling, federations typically assess thermal safety using empirical indices such as the Wet-Bulb Globe Temperature, recorded at discrete checkpoints or static start/finish locations via portable weather stations (UCI, 2023; Mountjoy et al., 2019). Nevertheless, static point measurements fail to resolve the highly variable thermal trajectory encountered by riders over hundreds of kilometers. To overcome this limitation, the Universal Thermal Climate Index (UTCI) offers a biophysically grounded framework that describes outdoor thermal conditions using 2-metre air temperature, humidity, wind, and radiation into an equivalent temperature scale (Bröde et al., 2012). Applied along a cycling route, it can reveal spatial and temporal contrasts that a stage mean or a small set of fixed observations may conceal. Its standard categories describe modelled environmental thermal stress; they should not be read as measurements of riders' body temperature or as sport-specific safety thresholds.

Importantly, the UTCI provides a dual analytical advantage for cycling competitions. For static trackside spectators, who remain on roadside for hours under direct solar exposure, the standard UTCI categories directly quantify experiential thermal strain and environmental risk. For elite riders, whose high work rates generate substantial internal metabolic heat, the UTCI serves as a reliable proxy of external atmospheric and radiative boundary conditions. In this study, we reconstruct UTCI along all 21 stages of the 2026 Tour de France using the peloton's estimated passage times, combining high-resolution

ERA5 reanalysis and WRF meso-scale atmospheric simulations corrected with observations from Meteocat and Meteofrance ground station networks. We examine how thermal conditions vary both within and between stages (1), identify routes with sustained or localised high values (2), and quantify the share of reconstructed distance and riding time in each UTCI category (3). In addition, WBGT was calculated to compare with UCI standards and assess differences between the two indices, informing their use in cycling decision-making (4). By coupling moving-route tracking with fine-scale biometeorological modelling, this study advances the assessment of heat vulnerability for both competitors and spectators in elite mobile sporting events.

2. Methods

2.1 Study design, stages and route data T

Environmental heat stress was retrospectively reconstructed across the 21 stages of the 2026 Tour de France, held from 4 to 26 July 2026. The stage catalogue provided the date, start and finish locations, nominal distance and type of each stage. The route set included a team time trial on stage 1, an individual time trial on stage 16, and flat, hilly and mountain stages (Figure 1). The principal unit of analysis was a location along a stage route paired with an estimated passage-time. Accordingly, the results describe modelled outdoor conditions along the course rather than an individual rider's exposure or physiological response.

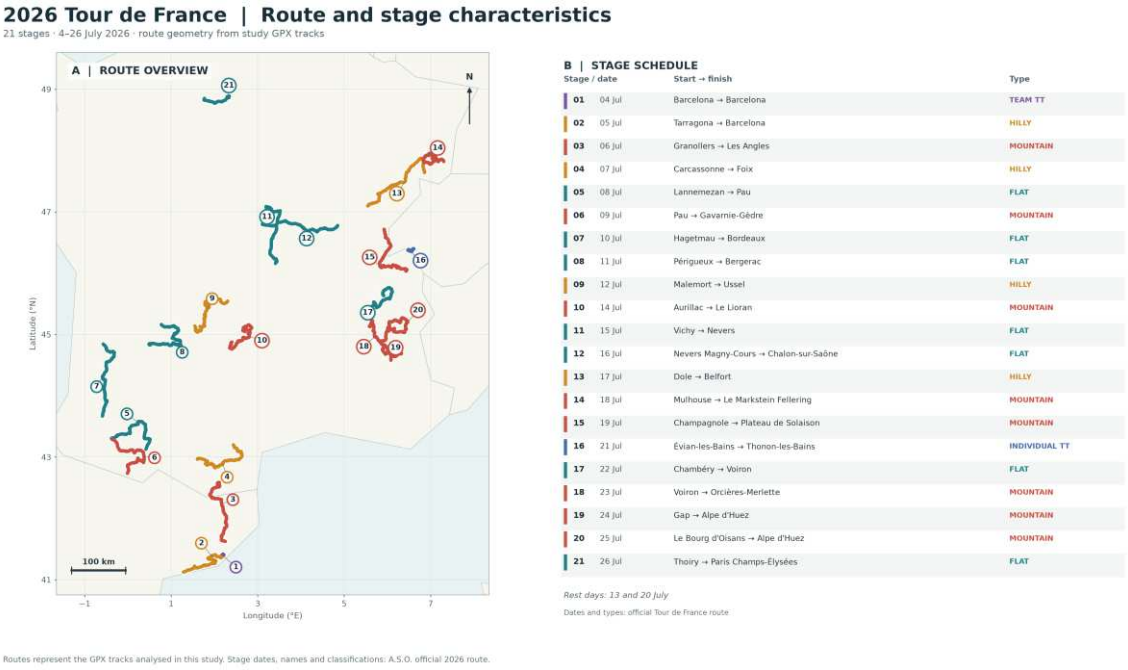


Figure 1. Stages of the Tour de France 2026 with date and type

Route geometry and elevation were obtained from stage-specific GPX tracks. Consecutive track points were joined to calculate cumulative great-circle distance using the haversine formula. Latitude, longitude, and GPX elevation were linearly interpolated at approximately 1 km intervals. The final route point was retained when the last interval

was shorter than 1 km. As last step, distances were derived from the GPX tracks rather than the rounded nominal distances in the stage catalogue.

2.2 Reconstruction of passage times

All timestamps used in the calculations were expressed in Coordinated Universal Time (UTC). A stage-specific schedule file supplied start and finish times where available. For stages without entered start and finish times, provisional schedules were generated by fixing the finish at 15:30 UTC and calculating the start time from GPX-derived route length and an assumed stage-level mean speed. The values of 43, 40 and 35 km h^{-1} for flat, hilly and mountain stages, respectively, were heuristic modelling choices intended to represent differences in expected stage duration; they were not calibrated against observed race speeds. A fallback of 38 km h^{-1} was applied to types not covered by these three categories, including the individual time trial. Consequently, estimated passage times and the meteorological conditions assigned to route points are sensitive to these assumptions.

Within each stage, we distributed the available start-to-finish duration across route segments according to a gradient-dependent relative speed profile. We calculated segment gradient from differences in GPX elevation, smoothed with a three-segment rolling median and bounded between −12% and +16%. The profile assigned longer travel times to climbs and shorter times to descents. Segment travel times were then rescaled so that their sum equalled the specified stage duration. The resulting estimated passage-time, elapsed time, gradient and implied speed were retained for each route point. This procedure reconstructs a plausible timetable; it does not establish the peloton's observed position. Passage times are particularly uncertain for the two-time trials, during which teams or individual riders started at different times.

2.3 ERA5 data and WRF simulation

ERA5 reanalysis supplied the atmospheric and land-surface input for the Weather Research and Forecasting (WRF) downscaling workflow (Hersbach et al., 2020; Skamarock et al., 2019). We requested hourly input for 3–27 July 2026 over a domain extending from 40.0 to 51.5° N and from 6.5° W to 11.5° E with a 0.25x0.25 original resolution. The pressure-level request comprised 37 levels and included geopotential, temperature, humidity, horizontal wind components, and vertical velocity. The single-level request included 2 m temperature and dew point, 10 m wind components, surface and mean sea-level pressure, skin and sea-surface temperature, land–sea mask, soil properties and soil temperature and moisture layers, snow depth, surface roughness and orography. Files were requested in GRIB format.

Simulations were organised by stage. ERA5 fields were processed through the WRF Preprocessing System using geogrid, ungrib and metgrid, followed by real and wrf (National Centre for Atmospheric Research, n.d.; Skamarock et al., 2019). The domain design specified a common outer d01 grid with nominal 9 km spacing, an intermediate D2 with 3km of grid and stage-centred innermost d03 grids with nominal 1 km spacing.

Meteorological extraction used the stage-specific wrfout_d03 files and accepted their recorded timestamps, which could differ in cadence between simulations (Fig-2).

For each sampled route location, we selected the nearest WRF grid cell classified as land using grid latitude and longitude. For each reconstructed passage time, we selected the temporally closest valid wrfout_d03 record. No spatial interpolation between WRF cells or temporal interpolation between WRF output records was applied at this step. We converted two-metre air temperature (T2) from kelvin to degrees Celsius. We calculated relative humidity from 2 m specific humidity (Q2), surface pressure (PSFC), and air temperature. We calculated wind speed from the 10 m components (U10 and V10) and applied a lower bound of 0.5 m s^{-1} in the thermal-index calculation. WRF terrain height (HGT) was retained for subsequent elevation correction.

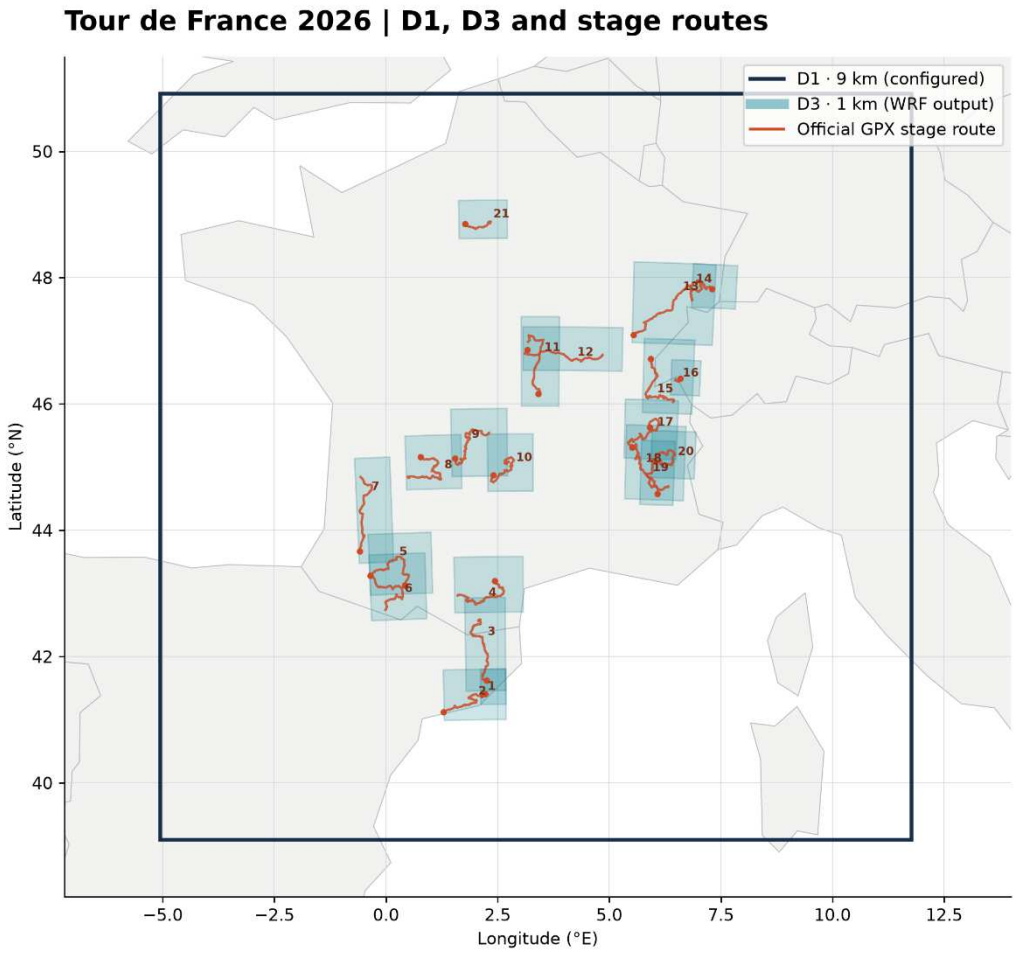


Figure 2. WRF domains for the 21 stages of the 2026 Tour de France. The D1 outline represents the configured 9 km domain, and the D3 outlines are derived from the latitude and longitude coordinates of the 1 km WRF outputs.

2.4 Météo-France and Meteocat observations and station selection

We obtained hourly Météo-France and Meteocat observations from compressed departmental CSV files. The source product provides station observations by department, with times expressed in UTC for metropolitan France (Météo-France, 2026) and the

XEMA (Xarxa d'Estacions Meteorològiques Automàtiques) of Servei Meteorològic de Catalunya- Meteocat for the three first stages in Catalonia (SMC, 2026). The selection routine read station identifier, name, coordinates, elevation, observation time, air temperature (T), relative humidity (U) and, when available, wind and radiation fields.

For each stage, we examined observations from one hour before its reconstructed start until one hour after its reconstructed finish (Fig. 3). We selected a station when its minimum great-circle distance to any GPX track point was no greater than 35 km and at least three temperature and humidity observations were available within that window. For selected stages, we used the routine read specified departments; otherwise, we scanned the available departmental files and retained one file per department. We wrote selected observations to a standardised table containing station metadata, meteorological values, and distance to the route. All 21 stage outputs used station-based calibration. We used observed temperature and relative humidity to correct the WRF fields. Station wind and radiation measurements were retained when available but were not used to adjust WRF wind or radiation. Although the input reader could import Météo-France quality-code columns.

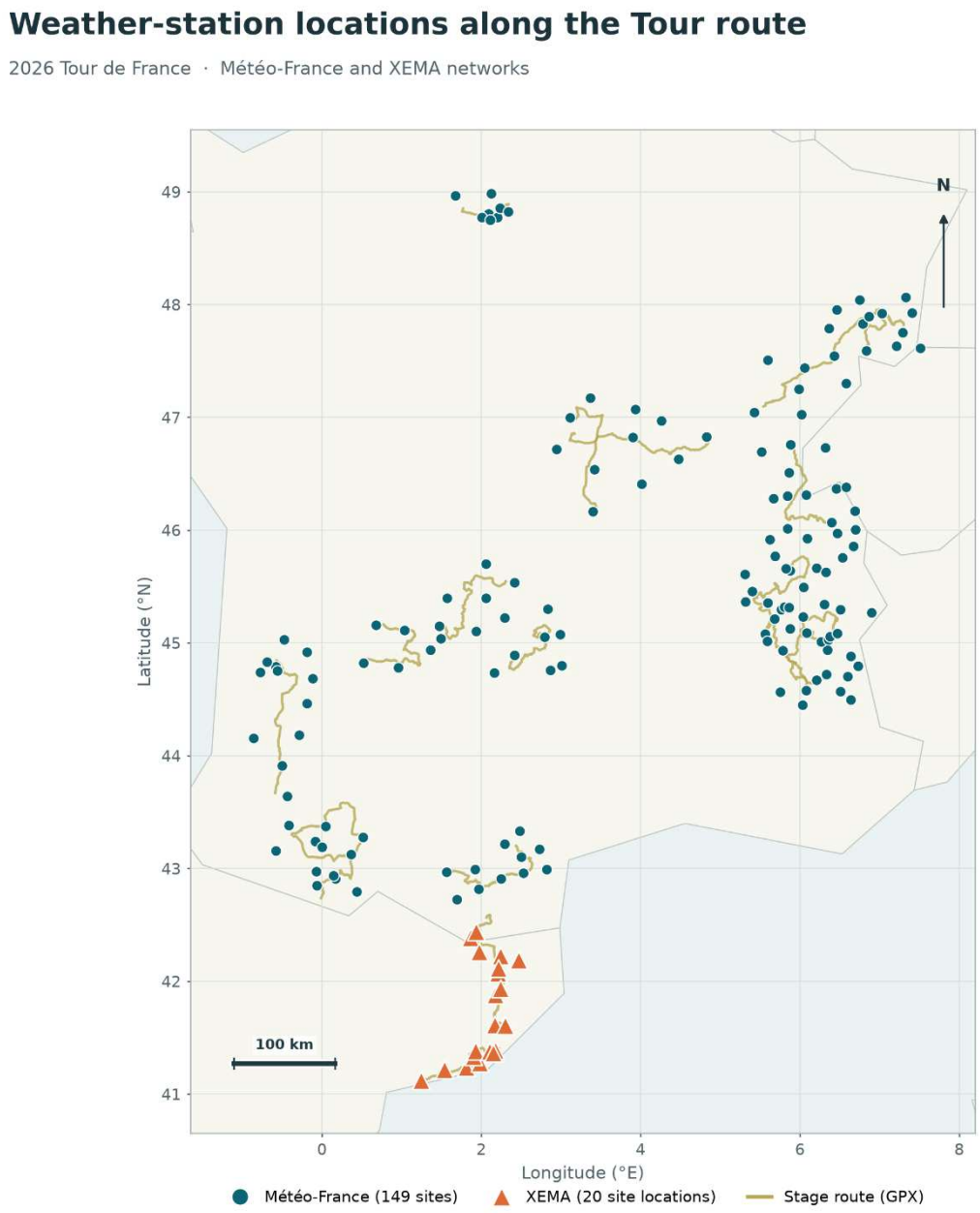


Figure 3. . Stations from Meteocat and Météo-France used for the correction

2.5 Observation-based bias correction

We paired each selected station with its nearest land WRF grid cell and the nearest kilometre along the stage route. For each station observation, we sampled the WRF output closest in time at the associated grid cell. Because station and model-grid elevations may differ, we adjusted observed air temperature to the WRF cell elevation before calculating model bias, following the approach used in previous WRF evaluations over complex terrain (Mues et al., 2018).

Using a fixed lapse rate of $\Gamma = 0.0065 \quad ^{\circ}\mathrm{C\,m^{-1}}$, the elevation-adjusted observation for station $i$at time $t$was calculated as

$$T^{*}_{\mathrm{obs},i}(t) = T_{\mathrm{obs},i}(t) - \Gamma\big(z_{\mathrm{WRF},i} - z_{\mathrm{station},i}\big),$$

where $z_{\mathrm{station},i}$is the station elevation and $z_{\mathrm{WRF},i}$is the elevation of its paired WRF cell. Temperature bias was then defined as the difference between the adjusted observation and WRF 2 m air temperature:

$$b_{T,i}(t) = T^{*}_{\mathrm{obs},i}(t) - T_{\mathrm{WRF},i}(t).$$

Relative-humidity bias was calculated without an elevation adjustment:

$$b_{\mathrm{RH},i}(t) = \mathrm{RH}_{\mathrm{obs},i}(t) - \mathrm{RH}_{\mathrm{WRF},i}(t).$$

These station-level bias series were stored separately for each stage. For each route point, we interpolated station biases to its estimated passage time and then along route distance. The resulting temperature correction also accounted for the difference between GPX elevation and WRF terrain height:

$$T_{\mathrm{corrected}}(x, t_x) = T_{\mathrm{WRF}}(x, t_x) + \hat{b}_T(x, t_x) - \Gamma[z_{\mathrm{GPX}}(x) - z_{\mathrm{WRF}}(x)],$$

At each route point, we linearly interpolated the bias series from each selected station to the estimated passage time. We then linearly interpolated the time-matched station biases along cumulative route distance between the kilometres associated with successive stations. Beyond the range covered by the selected stations, we carried the nearest station bias to the route endpoint. Using station observations to estimate and transfer model corrections to locations without observations follows a general approach used for bias-corrected WRF products, although we developed the route-based interpolation used here for this analysis (Holthuijzen et al., 2021).

We obtained corrected route temperature by adding the interpolated temperature bias to WRF T2 and adjusting for the elevation difference between the GPX route point and WRF terrain using the adopted lapse rate of 0.0065 °C m^{-1}. Accounting for differences between model and actual terrain elevation is particularly relevant when comparing or transferring WRF temperatures in complex terrain (Mues et al., 2018). We obtained corrected relative humidity by adding the interpolated humidity bias to the WRF estimate and constraining the result to 0–100%. Observation-based bias correction was applied to air temperature and relative humidity only, because the available station data were insufficient to support a reliable correction of wind speed and radiation across all stages. We tested a four-variable multivariate correction following Cannon (2018), but it did not improve validation performance and produced implausible cold-stress values, particularly on stage 21 and others, due to the absence of quality data. Wind speed and radiation were therefore retained from the uncorrected WRF fields.

When no eligible station observations were available, the code permitted a wrf_only mode with zero observational bias; none of the 21 current stage outputs used this mode. The same station observations were used to estimate the correction, so station–model differences calculated from them cannot be treated as independent validation. An independent evaluation would require withholding stations or observation times from calibration and reporting, for example, bias, mean absolute error and root mean square error. The fixed lapse rate, 35 km selection radius and interpolation rules were choices made for this study and require sensitivity assessment.

2.6 Mean radiant temperature and UTCI

Mean radiant temperature (MRT) was estimated from the WRF downward and upward shortwave fluxes (S↓ and S↑), downward and upward longwave fluxes (L↓ and L↑), and the cosine of the solar zenith angle (μ = COSZEN). All radiation fluxes were expressed in W m⁻². Because direct-normal shortwave radiation was unavailable, we first approximated the clearness index as:

$$"k" \ " = ""clip"\left(\frac{"S"}{"1361 \cdot ""max"("μ, 0.01")}", 0, 1.2"\right)$$

The hourly Erbs et al. (1982) relationship was used to calculate the diffuse fraction, kd:

$$"k" \ " = \begin{cases} "1 - 0.09""k" & "kt \leq 0.22" \\ "0.9511 - 0.1604""k" \ " + 4.388""k" \ " - 16.638""k" \ " + 12.336""k" & "0.22 < kt \leq 0 \\ "0.165" & "kt > 0.80" \end{cases}$$

Diffuse and direct horizontal radiation were obtained from the diffuse fraction:

$$"S" \ " = ""clip"("k" \ "S" \ ", 0, ""S" \ ")$$

$$"S" \ " = ""S" \ " - ""S"$$

The direct-normal component was approximated by dividing the direct horizontal flux by μ when μ exceeded 0.10. At lower solar angles, the implementation retained the direct horizontal flux to avoid division by a small cosine:

$$"I" \ " = " \begin{cases} \frac{"S"}{"μ"} & "μ > 0.10" \\ "S" & "μ \leq 0.10" \end{cases}$$

Solar elevation (γ, in degrees) determined the projected-area factor following the formulation used by Di Napoli et al. (2020):

$$"γ = " \frac{"180"}{"π"} "arcsin"("clip"("μ, 0, 1"))$$

$$"f" \ " = 0.308""cos"\left(\frac{"πγ"}{"180"}\left("0.998 - " \frac{"γ"}{"50000"}\right)\right)$$

With equal upper- and lower-hemisphere view factors, shortwave absorptivity 0.70, and body-surface emissivity 0.97, the effective radiative flux and MRT were:

$$"Q" \ " = "\frac{"L" \ " + ""L"}{"2"}" + "\frac{"0.70"}{"0.97"}\left(\frac{"S" \ " + ""S"}{"2"}" + ""f" \ "I" \ \right)$$

$$"T" \ " = "\left(\frac{"Q"}{"σ"}\right) \ " − 273.15"$$

Here $\sigma = 5.670374419 \times 10^{-8}$ W m^{-2} K^{-4}. The 1361 W m^{-2} solar constant and the low-sun rule are implementation approximations. The WRF grid does not resolve roadside shade or sheltering between riders.

UTCI was calculated using the polynomial approximation in pythermalcomfort, with corrected air temperature, vapour pressure derived from corrected humidity, WRF 10 m wind speed and the difference between MRT and air temperature as inputs (Bröde et al., 2012; Tartarini & Schiavon, 2020). Both indices were expressed as equivalent temperatures in degrees Celsius.

UTCI values were assigned to the following standard categories: no thermal stress, 9–<26 °C; moderate heat stress, 26–<32 °C; strong heat stress, 32–<38 °C; very strong heat stress, 38–<46 °C; and extreme heat stress, ≥46 °C. We retained categories below 9 °C in the processing code as cold-stress categories (Bröde et al., 2012). These classifications describe environmental conditions under the UTCI reference model. They are not athlete-specific clinical thresholds or direct estimates of heat illness probability.

Outdoor wet-bulb globe temperature (WBGT) was estimated at approximately 1 km intervals along each stage using the physical model of Liljegren et al. (2008). Station-corrected air temperature and relative humidity were combined with WRF D3 surface pressure, downward shortwave radiation and solar zenith geometry at the assigned cell and time. Surface pressure was adjusted from WRF terrain elevation to GPX route elevation. The direct fraction of shortwave radiation was estimated from the clearness index using Erbs et al. (1982). Following the UCI (UCI, nd) practical guide, reconstructed peloton speed was used as the air-speed input. Natural wet-bulb and globe temperatures were solved iteratively and combined to obtain outdoor WBGT. Point values were compared with the UCI bands: white (<15 °C), green (15–<18 °C), yellow (18–<23 °C), orange (23–<28 °C) and red (≥28 °C). One point with corrected relative humidity of 0% was excluded. Peloton speed was estimated rather than observed; ambient wind direction and rider sheltering were not resolved.

Peloton air speed

The estimated speed at each route point was converted from km h^{-1} to m s^{-1}:

$$v_{\mathrm{p}} = \frac{v_{\mathrm{est}}}{3.6}$$

Pressure at route elevation

An isothermal hypsometric approximation was used to adjust WRF surface pressure from model terrain elevation to GPX route elevation:

$$p_{\mathrm{route}} = p_{\mathrm{WRF}} \exp\left(-\frac{g(z_{\mathrm{route}} - z_{\mathrm{WRF}})}{R_{\mathrm{d}}(T_{\mathrm{a}} + 273.15)}\right)$$

Direct solar fraction

The clearness index was calculated from WRF downward shortwave radiation (SWDOWN) and the non-negative cosine of solar zenith angle (μ). The diffuse fraction was estimated with the Erbs relationship:

$$k_{\mathrm{T}} = \mathrm{clip}\left(\frac{\mathrm{SWDOWN}}{\max(1361\mu, 0.001)}, 0, 1.2\right)$$

$$k_{\mathrm{d}} = \begin{cases} 1 - 0.09k_{\mathrm{T}} & \mathrm{kT} \le 0.22 \\ 0.9511 - 0.1604k_{\mathrm{T}} + 4.388{k_{\mathrm{T}}}^2 - 16.638{k_{\mathrm{T}}}^3 + 12.336{k_{\mathrm{T}}}^4 & 0.22 < \mathrm{kT} \le 0.80 \\ 0.165 & \mathrm{kT} > 0.80 \end{cases}$$

$$f_{\mathrm{dir}} = 1 - k_{\mathrm{d}}$$

The direct fraction was set to zero when the Sun was below the model's zenith threshold and was capped at 0.9 for the Liljegren solver.

Outdoor WBGT

The Liljegren energy balances yielded natural wet-bulb temperature (Tnwb) and globe temperature (Tg). Outdoor WBGT was then calculated as:

$$\mathrm{WBGT} = 0.7T_{\mathrm{nwb}} + 0.2T_{\mathrm{g}} + 0.1T_{\mathrm{a}}$$

Here Ta is the station-corrected 2 m air temperature. All temperatures in the WBGT equation are expressed in °C. The UCI bands were applied to individual route-point estimates, not to stage means.

2.7 Stage profiles, maps and synthesis

Each GPX route was sampled at approximately 1-km intervals along cumulative distance, including the final endpoint. The interval between the stage start and finish times was distributed among consecutive route segments according to a gradient-dependent relative speed profile. This produced an estimated UTC passage time for every sampled point. For each point, meteorological variables were taken from the nearest land cell of the WRF d03 domain and the WRF output time closest to its estimated passage time. Station-derived temperature and relative-humidity biases were interpolated in time and along cumulative route distance; air temperature was also adjusted for the elevation difference between the route and the WRF cell. UTCI and WBGT were then calculated separately at each point from the corrected temperature and humidity, WRF wind speed and

estimated mean radiant temperature. The WRF wind and radiation fields were not corrected with station observations.

For mapping and category-based exposure, the value assigned to each segment between consecutive points was the arithmetic mean of its two endpoint values. The entire segment length (the difference in cumulative kilometres) and reconstructed travel time (the difference between endpoint passage times) were assigned to the UTCI and WBGT categories of that segment mean. Segment lengths and durations were summed by category for each stage, and percentages were calculated against the total length and duration of segments with valid values. Overall category totals were obtained by summing across all 21 stages. Stage minimum, maximum and mean values were calculated from the sampled points; the reported mean is an arithmetic point mean, not a distance-weighted or time-weighted exposure mean.

4. Results

4.1 Thermal conditions across the 2026 Tour de France

The reconstructed analysis covered all 21 stages of the 2026 Tour de France and approximately 3,323 km of route, sampled in ~1 km segments. As shown in table 2, strong heat stress accounted for 1,147 km, very strong heat stress for 862 km, and no segments reached the extreme heat stress category (≥ 46 ˚C). Combined, strong and very strong heat stress represented approximately 60.5% of the analysed distance (2,009 km). The corresponding time-based classification placed approximately 57.8% of reconstructed riding time in strong heat stress or above (2,991 min).

Table 1. Reconstructed route distance and riding time by UTCI category across the 21 stages of the 2026 Tour de France

UTCI category	Distance (km)	Share of distance (%)	Time (min)	Share of time (%)
No thermal stress (<26 °C)	441.3	13.28	729.8	14.12
Moderate heat stress (26–<32 °C)	872.6	26.26	1,451.70	28.06
Strong heat stress (32–<38 °C)	1,146.90	34.51	1,740.40	33.64
Very strong heat stress (38–<46 °C)	862.5	25.95	1,251.10	24.18
Extreme heat stress (≥46 °C)	0	0	0	0
Total	3,323.30	100	5,173.00	100

Conversely, evaluation under the sports-regulatory framework using the Wet-Bulb Globe Temperature (WBGT; Table 3) demonstrated that no stage segment reached or exceeded the critical threshold of 32.2 °C (black category), which mandates stage cancellation, postponement, or route truncation under the UCI Extreme Weather Protocol. However, 175.9 km of the route (5.3% of total distance; 254.8 min of riding time) fell within the Red WBGT category (≥28 °C), denoting high physiological risk where active cooling countermeasures and unrestricted feeding zones are recommended. The vast majority of the route fell within the Orange (23–<28 °C; 53.6%) and Yellow (18–<23 °C; 37.8%) categories.

Table 2. Route distance and riding time by WGBT-UCI category across the 21 stages of the 2026 Tour de France

WBGT category	WBGT (°C)	Distance (km)	Distance (%)	Time (min)	Time (%)
White	<15	30	0.9	46.67	0.9
Green	15–<18	79.4	2.39	145.3	2.81
Yellow	18–<23	1,255.9	37.8	2,065.1	39.93
Orange	23–<28	1,781.6	53.6	2,660.2	51.43
Red	≥28	175.8	5.29	254.8	4.93
Total valid		**3,322.9**	**100**	**5,172.0**	**100**

This divergence between indices highlights the distinction between regulatory threshold compliance and cumulative environmental burden. While riders traversed the 175.9 km of high-risk WBGT conditions relatively quickly, trackside spectators remained stationary along these identical corridors (particularly across stages 4, 7, 8, and 9) for hours during peak afternoon solar irradiance, experiencing sustained ambient conditions in the upper tiers of UTCI (38–44 °C).

The maps show (Fig.4) substantial variation both between regions and along individual stages. In Catalonia (A), the coastal sections of stages 1 and 2 are among the warmest parts of the route, whereas stage 3 cools as it moves north. The Barcelona detail (H) makes the variation within the opening stages easier to see: temperature and UTCI change over short distances, even within the metropolitan area.

In the Pyrenees and Occitanie (B), stage 4 stands out for its high UTCI, while the mountain sections show lower values. The Southwest and Massif Central (C) contain several extended warm sections across stages 7–10, with particularly high UTCI on parts of stages 8 and 9. Central France and Burgundy (D) remain broadly warm, although the southern portion of stage 11 is cooler than the rest of that regional route.

The Jura and Vosges (E) show mostly intermediate values and a gradual change along stage 13. The Alps (F) have the strongest association between the mapped relief and thermal conditions: cooler high-elevation sections occur close to warmer lower-elevation sections, producing marked variation within stages 15–20. The Paris stage (G) has comparatively low UTCI throughout its route. The Lake Geneva detail (I) also shows lower values than the hottest regions, with modest changes along the short section displayed.

2026 Tour de France | regional temperature and UTCI along the route

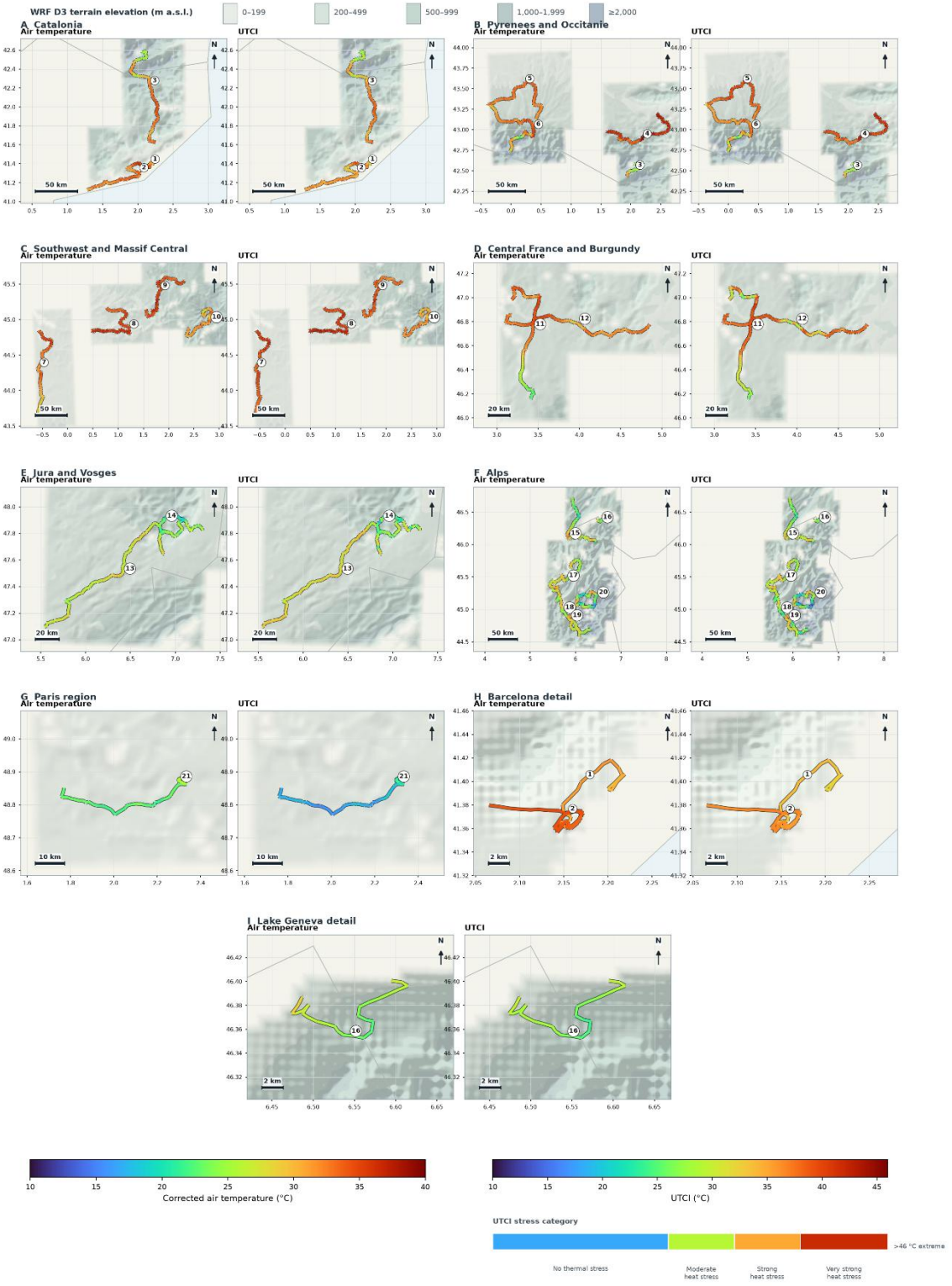


Figure 4.Regional distribution of modelled Temeprature and Universal Thermal Climate Index (UTCI) along the 21 stages of the 2026 Tour de France. Panels show Catalonia (A), the Pyrenees and Occitanie (B), the southwest and Massif Central (C), central France and Burgundy (D), the Jura and Vosges (E), the Alps (F), the Paris region (G), and enlarged views of Barcelona (H) and Lake Geneva (I). Each route segment is coloured according to the arithmetic mean of the UTCI values at its endpoints, using the UTCI ranks bands shown in the legend. .

The regional WBGT maps (Fig. 4) show a different pattern from the UTCI maps. Orange WBGT conditions (23–<28 °C) extend across much of the lowland route, particularly in Catalonia, the southwest and Massif Central, and central France. Red conditions (≥28 °C) appear in shorter sections, most visibly in the Pyrenees and southwest, rather than along entire stages. The Jura and Vosges show a transition from orange in lower terrain to yellow (18–<23 °C) at higher elevations. In the Alps, yellow conditions predominate, with some green sections on mountain routes; the Paris stage is also mainly yellow.

Across all stages, the orange and red WBGT bands account for 53.6% and 5.3% of valid route distance, respectively. These colours should not be equated with similarly named UTCI stress categories: the indices use different calculations and thresholds. WBGT incorporates the corrected temperature and humidity, modelled radiation, and the expected peloton speed, so differences between the two maps are expected, especially where elevation and exposure change along a stage.

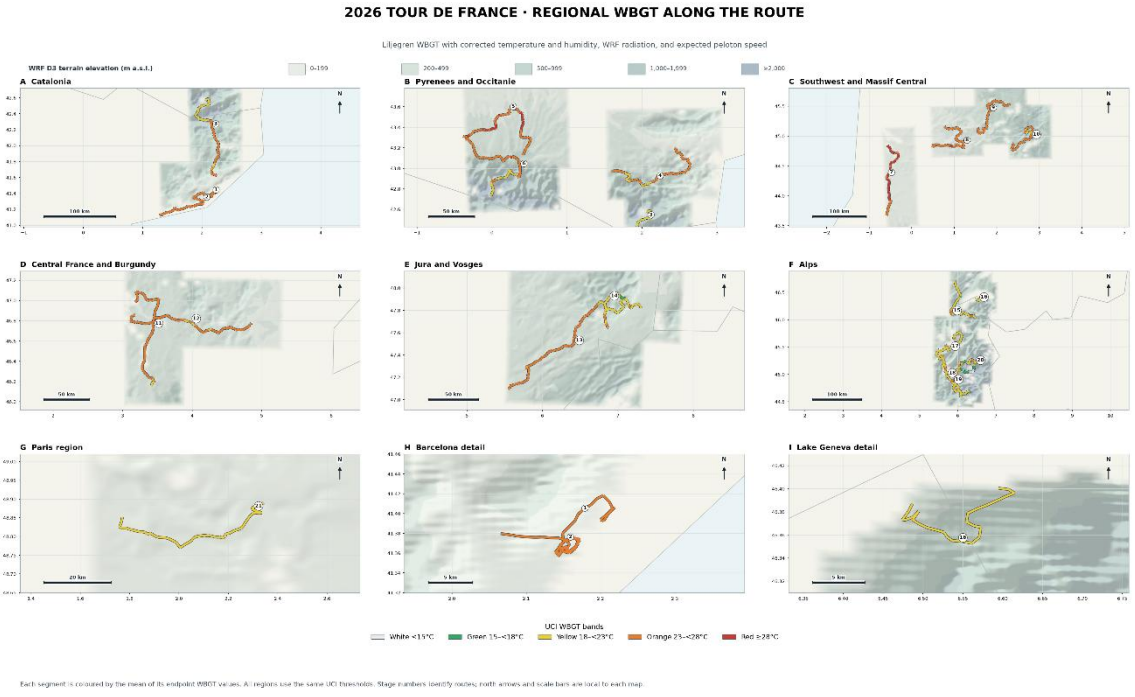


Figure 5. Regional distribution of modelled wet-bulb globe temperature (WBGT) along the 21 stages of the 2026 Tour de France. Panels show Catalonia (A), the Pyrenees and Occitanie (B), the southwest and Massif Central (C), central France and Burgundy (D), the Jura and Vosges (E), the Alps (F), the Paris region (G), and enlarged views of Barcelona (H) and Lake Geneva (I). Each route segment is coloured according to the arithmetic mean of the WBGT values at its endpoints, using the UCI WBGT bands shown in the legend.

4.2 Variation between stages

Stage mean UTCI ranged from 21.3 °C on stage 21 to 41.3 °C on stage 8 (Fig. 6). Stage 4 had a mean UTCI of 39.8 °C and contained the highest tabulated route value, 44.5 °C, on the Carcassonne–Foix stage (near km 81). Stage 7 had a mean UTCI of 39.5 °C, while stages 5 and 9 averaged 38.5 °C and 38.3 °C, respectively. Stage 3 also presented substantial heat load, averaging 37.8 °C with peaks up to 44.3 °C. Under Di Napoli et al.'s (2020) refined radiant balance formulation, no route segment exceeded the extreme heat stress threshold of 46 °C, and maximum conditions across the race remained within the upper boundary of very strong heat stress.

Stage mean WBGT ranged from 18.1 °C on stage 20 to 28.5 °C on stage 7 (Fig. 4). Thus, the stage with the highest mean WBGT differed from the stage with the highest mean UTCI. Stage 7 also had the highest point-level WBGT, at 30.2 °C. Stages 5 and 8 had mean WBGT values of 27.6 °C and 27.2 °C, respectively, whereas stage 4 averaged 24.6 °C. These differences reflect the distinct calculations and classification thresholds of the two indices; their numerical values and colour categories are not directly interchangeable.

Mean UTCI declined across much of the latter part of the race, although individual stages remained heterogeneous. For example, stage 20 had a mean UTCI of 24.7 °C but ranged from 11.3 °C to 35.3 °C along the route (Fig. 4). Its mean WBGT was 18.1 °C, with values ranging from 11.6 °C to 24.0 °C (Fig. 5). Stage 21 had the lowest mean UTCI (21.3 °C; range: 16.5–26.5 °C), with a mean WBGT of 20.8 °C. These differences describe the environmental conditions assigned to each route at its reconstructed passage times and should not be interpreted as differences in riders’ physiological responses.

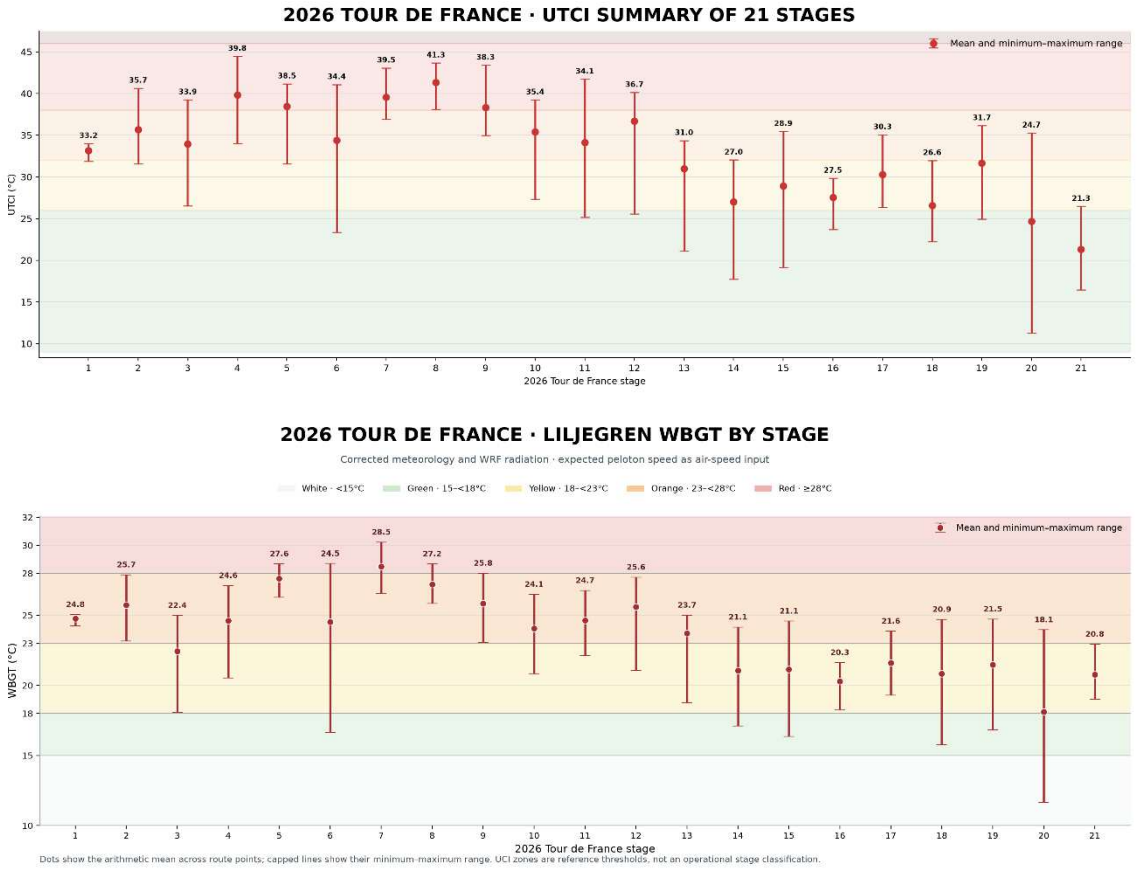


Figure 6. Stage-level thermal conditions during the 2026 Tour de France. Mean UTCI and WBGT for each stage (points), with vertical bars showing the minimum and maximum values along the reconstructed route. Numbers above the points

The stage means and standard deviations complement the minimum–maximum ranges by showing how widely the sampled values vary around each stage mean (Fig. 7). Stage 8 had the highest mean UTCI, 41.3 ± 1.3 °C, indicating consistently high values along its route. Stage 4 combined a high mean (39.8 ± 2.2 °C) with the highest individual UTCI value (44.5 °C). In contrast, stage 20 had a lower mean (24.7 °C) but the largest UTCI standard deviation (5.8 °C), consistent with the pronounced changes visible in its route profile. These standard deviations describe variation among sampled route points; they do not quantify uncertainty in the meteorological reconstruction.

For WBGT, stage 7 had the highest mean, 28.5 ± 0.8 °C, followed by stage 5 (27.6 ± 0.5 °C) and stage 8 (27.2 ± 0.6 °C). These small standard deviations indicate relatively uniform WBGT values along those stages. Stage 20 had the lowest mean WBGT (18.1 °C) and the largest WBGT standard deviation (3.2 °C), reflecting substantial variation along its mountainous route. For both indices, standard deviations describe variation among sampled route points; they do not quantify uncertainty in the meteorological reconstruction.

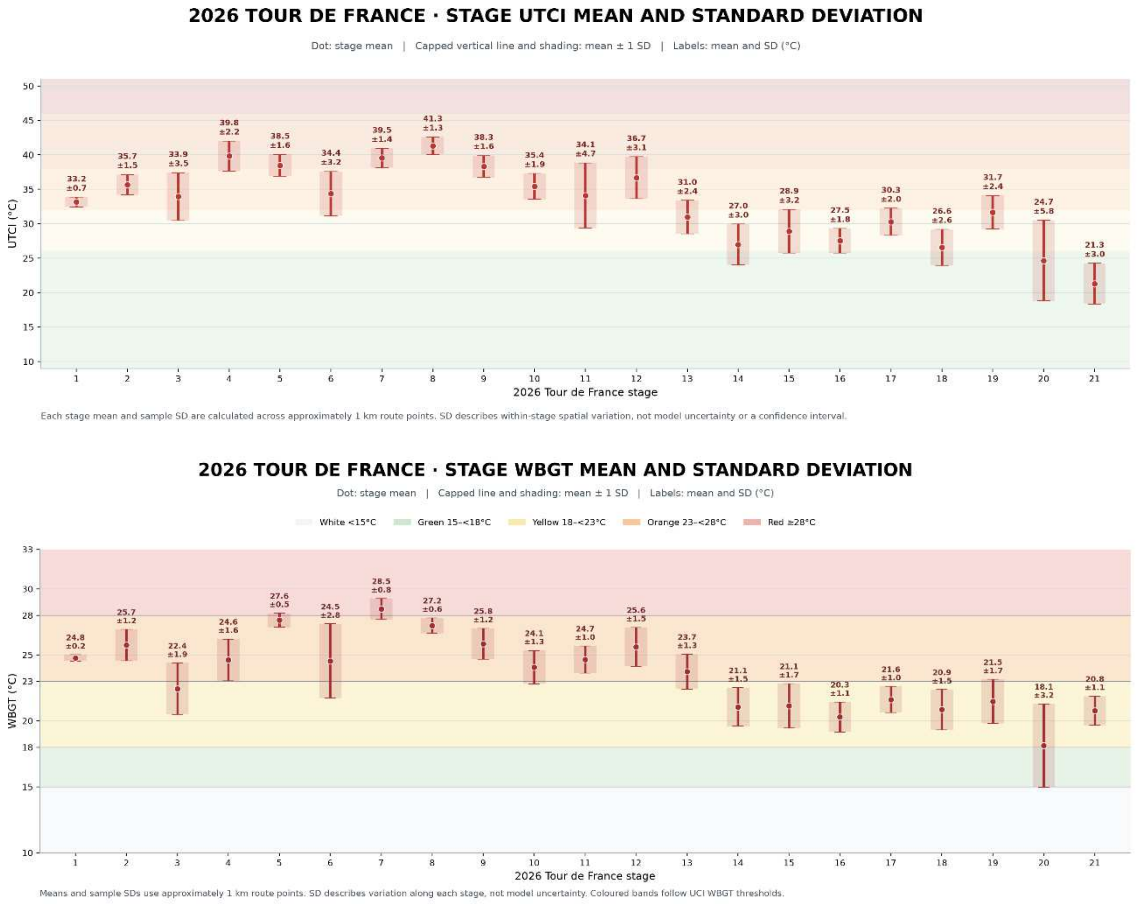


Figure 7. Stage level mean and SD for the 2026 Tour de France

4.3. Contrasting thermal profiles along individual stages

The UTCI profiles reveal marked differences both between and within stages. The most sustained heat stress occurred during stages 4, 5, 7, 8, and 9. In stage 8, every sampled route point fell within the very strong heat stress category (38–46 °C), with UTCI ranging from 38.1 to 43.7 °C. This category also accounted for approximately 79% of sampled points in stage 4 and 85% in stage 7. Stage 4 reached the highest UTCI value of the Tour (44.5 °C), although no sampled point exceeded the 46 °C threshold for extreme heat stress. From stage 13 onward, no sampled point reached the very strong heat stress category. These later profiles were generally cooler, but some changed substantially along the route. Stage 20 had the widest UTCI range (11.3–35.3 °C), crossing from no thermal stress into strong heat stress; its stage mean was 24.7 °C. By contrast, stage 21 was comparatively stable and 95% of its sampled points fell within the no thermal stress category. These profiles describe estimated conditions along each route at the reconstructed passage times. Differences between stages therefore reflect their combined locations, terrain and timing, rather than an isolated effect of elevation.

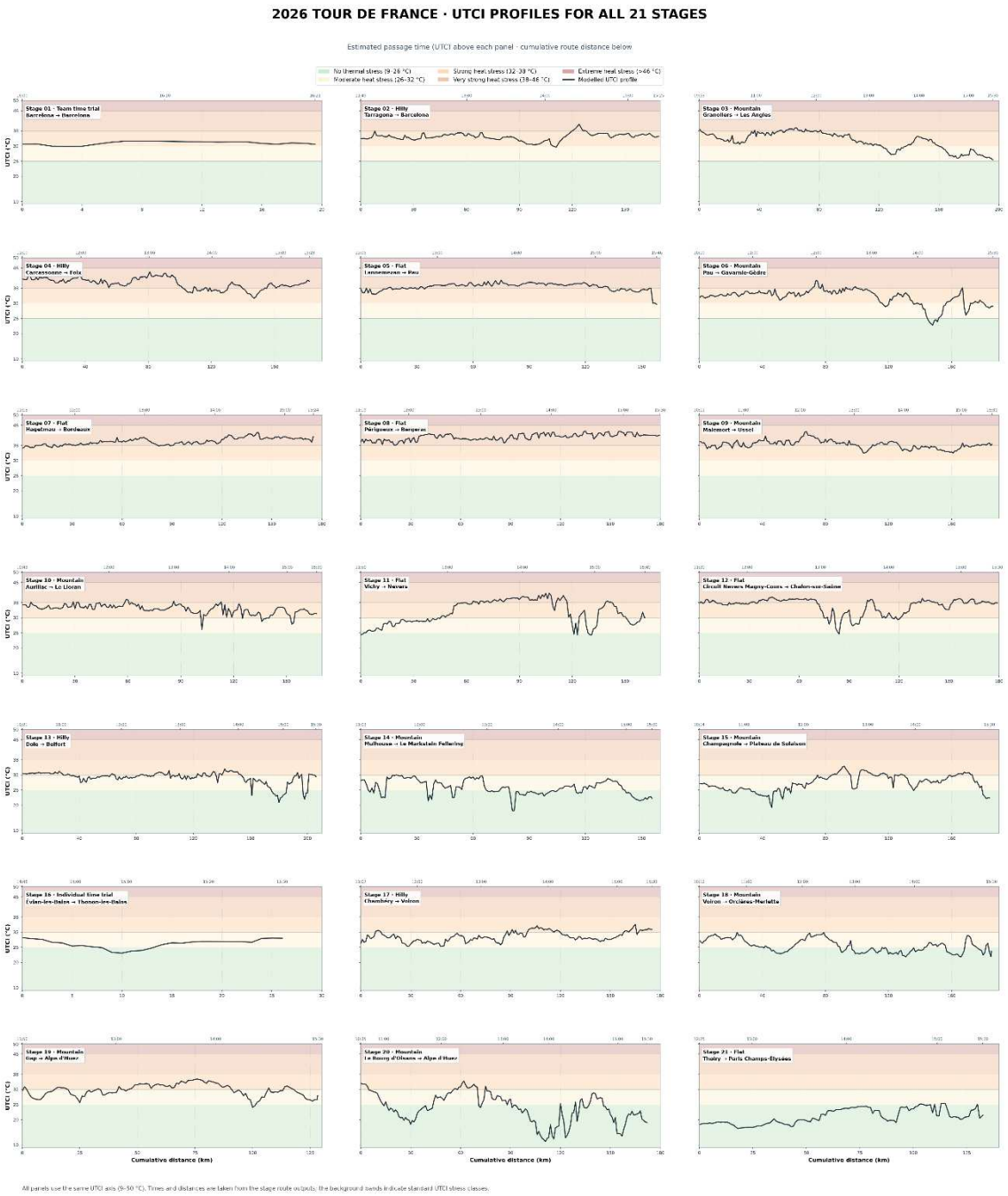


Figure 8. UTCI profiles along all 21 stages of the 2026 Tour de France. Curves show corrected UTCI estimates at approximately 1 km intervals against cumulative route distance; the upper axes indicate estimated passage time in UTC. Shaded bands represent the standard UTCI thermal stress categories. All panels share the same UTCI scale (9–50 °C) to support comparison between stages.

The WBGT profiles reveal both sustained exposure and rapid changes within individual stages (Fig. 9). Stage 7 remains predominantly in the red WBGT band (≥28 °C), whereas stages 5 and 8 approach or briefly enter that band. Stage 4, despite having one of the highest UTCI profiles, lies mainly in the orange WBGT band (23–<28 °C). This difference is also apparent in the stage rankings: stage 8 has the highest mean UTCI, while stage 7 has the highest mean WBGT.

The mountain profiles show greater variation along the route. WBGT falls markedly during stages 3 and 20, with stage 20 reaching the green and white bands in its cooler sections. Its UTCI profile likewise shows a pronounced decline, although the two indices assign different values and categories to the same route. Stage 21 has a comparatively steady WBGT profile, mainly in the yellow band. The profiles therefore add detail to the stage averages by showing where thermal conditions change during the reconstructed passage; UTCI and WBGT categories should be interpreted within their respective scales.



Figure 9. ***Modelled WBGT profiles along all 21 stages of the 2026 Tour de France.*** *The black line shows point-level WBGT against cumulative route distance; estimated passage time in UTC is shown above each panel. Shaded backgrounds indicate the UCI WBGT bands: white (<15 °C), green (15–<18 °C), yellow (18–<23*

°C), orange (23–<28 °C), and red (≥28 °C). All panels share the same WBGT axis to allow comparison among stages

The profiles reveal pronounced differences in thermal exposure across the 21 stages. Stages 4 and 7–9 show sustained high UTCI over substantial portions of their routes; stage 8 is especially notable for persistent very strong heat stress despite its relatively low elevation. Warm conditions also extend across several sections of stages 10–12, although their UTCI varies more along the route.

The mountain stages show a different pattern. On stages 3 and 6, UTCI generally falls as the route reaches higher elevations, while stage 20 has the clearest contrast between lower sections and its highest climb. This relationship is not uniform: changes in UTCI also occur at similar elevations, indicating that altitude alone does not explain the modelled conditions. Among the later stages, 13–19 contain a mixture of moderate and stronger heat-stress sections. Stage 21 stands apart with the lowest UTCI and a route classified predominantly as having no thermal stress.

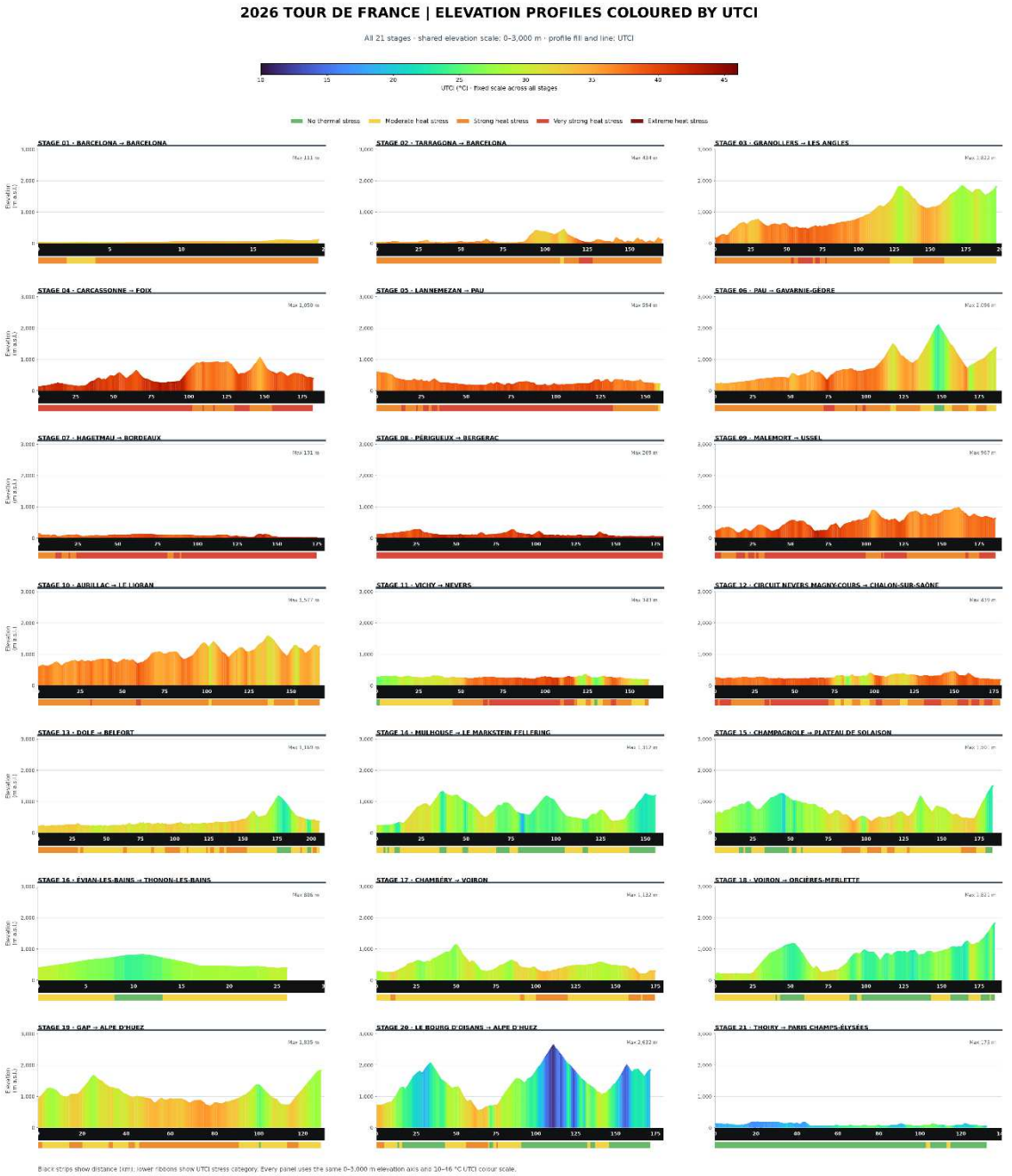


Figure 10. ***Elevation profiles of the 21 stages of the 2026 Tour de France, coloured by UTCI.*** *The filled area shows route elevation against cumulative distance; its colour represents the mean UTCI at the endpoints of each route segment. All panels use the same 0–3,000 m elevation scale and the same UTCI colour scale. The narrow black strip shows distance in kilometres. Stage numbers and maximum route elevations are indicated in each panel, and the legend identifies the UTCI thermal stress categories.*

The elevation profiles show where WBGT changes occur along each stage (Fig. 11). Low-elevation stages 7 and 8 maintain high WBGT over much of their length, including red-band sections, despite limited changes in terrain height. In mountain stages 3, 6, and 20, cooler WBGT values generally coincide with higher parts of the route. Stage 20 shows the clearest contrast: its line shifts towards cooler colours during the major climbs, while lower sections are warmer.

The corresponding UTCI figure also shows strong variation on mountain stages, particularly stage 20, but the colour transitions do not represent equivalent levels of stress. For example, stage 4 is prominent among the high-UTCI stages, whereas its WBGT profile remains largely within the orange band. Viewed together, the figures show how each index changes along the same terrain profile. Elevation is useful context for these changes, although weather conditions and reconstructed passage time also vary along the route.

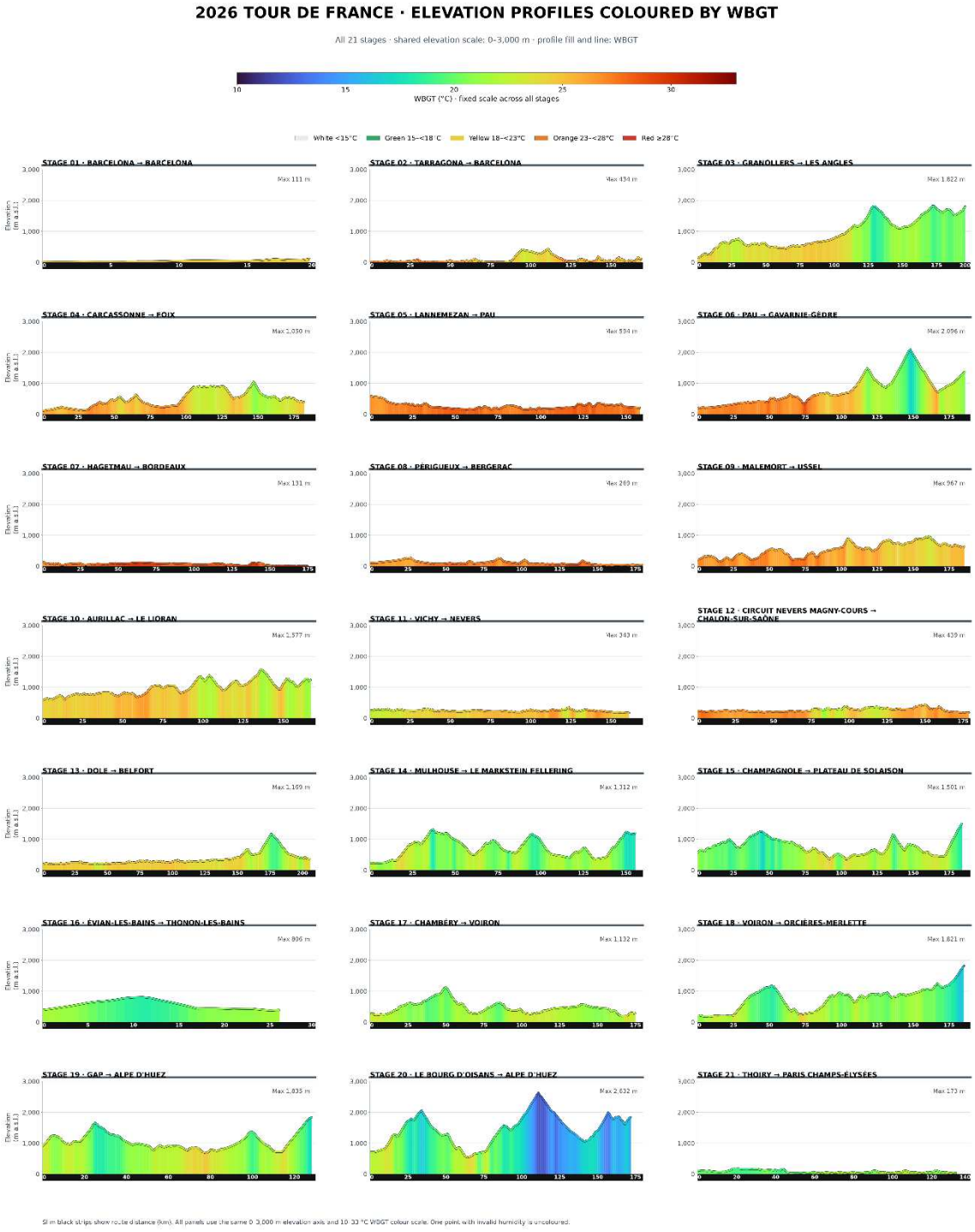


Figure 11. ***Elevation profiles of the 21 stages of the 2026 Tour de France, coloured by WBGT.*** **The filled area shows route elevation against cumulative distance; its colour represents the mean modelled WBGT at the endpoints of each route segment. All panels use the same 0–3,000 m elevation scale and the same**

WBGT colour scale. The narrow black strip shows distance in kilometres. Stage numbers and maximum route elevations are indicated in each panel, and the legend identifies the UCI WBGT bands

5. Discussion

5.1 Spatiotemporal exposure dynamics and the WBGT–UTCI divergence

The route-based reconstruction and analysis indicates substantial variation in environmental heat stress across the 2026 Tour de France, with approximately 60.5% of reconstructed route distance (2,009 km) and 57.8% of estimated riding time (2,991 min) fell within strong heat stress or higher UTCI categories (≥ 32ºC). The parallel WBGT assessment reveals a stark regulatory divergence: no single route segment reached the UCI Extreme Weather Protocol's cancellation threshold of 32.2 °C, yet over 175 km occurred under high-risk Red category conditions (WBGT ≥28 °C).

However, this study reinforces the need to perform the computation of these thermal comfort indices considering thee shifting conditions of microclimatic conditions along the route, and not only in specific checkpoints, such as when the stage starts or finishes (UCI, 2023). The UTCI provides a biophysically superior framework, because it integrates mean radiant temperature, humidity, and wind into the equation (Bröde et al., 2012). Therefore, while WBGT confirms regulatory compliance across the 2026 route, modeling UTCI reveals the actual atmospheric burden: cyclists spent nearly 50 hours of racing under strong or very strong UTCI heat stress, operating within an environment characterized by severe resistance to metabolic heat dissipation.

5.2 Topographical heat traps, peloton dynamics, and physiological strain

Thermal conditions were distributed unevenly during the Tour and the stages themselves. Some stages experienced sustained high values, while others crossed several thermal categories within a single route. Pairing meteorological conditions with estimated passage times therefore provides information that a stage mean or a fixed-location observation cannot convey.

The contrast between stages 4 and 8 illustrates the difference between a peak and sustained heat stress. Stage 4 had the highest tabulated UTCI (44.5 °C near km 81), whereas stage 8 had the highest stage mean (41.3 °C) and remained in the very strong heat stress category throughout its reconstructed route, with 100.0% of its 179.8 km. Stage 20 showed a different pattern, with pronounced changes in UTCI along the route, ranging from 11.3 °C at high altitude to 35.3 °C in the valleys. These profiles suggest examining the duration and location of elevated values alongside the maximum recorded for each stage.

These spatial patterns coincide directly with known physiological strain mechanisms in endurance cycling. Under sustained power outputs of 250–350 W, elite cyclists generate in excess of 1,000 W of internal metabolic heat that must be cleared across a rapidly narrowing skin-to-ambient thermal gradient (Périard et al., 2021). When riding through low-albedo asphalt corridors and enclosed valleys where reflected long-wave radiation is

elevated, sensible heat loss reverses, forcing near-exclusive reliance on sweat evaporation. However, aerodynamic investigations reveal that drafting within a dense peloton attenuates air velocity around mid-pack riders by up to 50–70% (Blocken et al., 2018), drastically blunting convective dissipation while collective sweat rates saturate the local boundary layer. Furthermore, during steep mountain ascents (such as those traversed in stage 20), riding speed drops precipitously to 15–20 km/h precisely when metabolic work peaks (>400 W), triggering rapid uncompensable heat storage and threatening core temperatures (Tcore > 39.5ºC) associated with central fatigue and exertional heat illness (Roberts et al., 2023; Valenzuela et al., 2022).

5.3 Methodological strengths and limitations

Our findings complement those of Cvijanovic et al. (2026), who documented increasing July heat stress across France and highlighted the difficulty of describing a moving peloton's conditions using observations at fixed locations and hours. Their analysis used Wet-Bulb Globe Temperature (WBGT), whereas the present study also uses UTCI to reconstruct conditions along the routes of a specific edition. The numerical values and thresholds of the two indices are not directly comparable. The present analysis adds spatial and temporal detail by estimating when each route location was traversed. It quantifies both distance and time within thermal stress categories.

This focus on exposure timing is also consistent with research on other outdoor activities. Olano Pozo et al. (2024) assessed heat during scheduled castells performances and found rising temperatures during event hours at four locations in Catalonia. The Tour de France presents a different challenge because the activity moves through changing environments. Reconstructed passage times allow us to examine these changes, although distance- and time-based category shares may differ because travel speed varies.

The analysis has several limitations. We reconstructed passage times rather than measuring them continuously. Uncertainty in stage schedules and gradient-dependent speed estimates may affect the meteorological conditions assigned to individual segments, particularly during periods of rapid daily change. This limitation is greater for the team and individual time trials, when riders or teams pass the same point at different times. Alternative passage-time scenarios should therefore be used to test the stability of the stage profiles and category shares.

The meteorological fields also cannot resolve every condition immediately surrounding a rider. Local shade, vegetation, buildings, road surfaces and airflow may produce differences from the conditions represented by a WRF grid cell. Meteorological station observations were used to correct air temperature and relative humidity, but the current workflow did not correct wind or radiation. Furthermore, observations used for calibration do not constitute independent validation; that assessment requires stations or observation periods withheld from the correction procedure.

To reduce radiative uncertainty, we reconstructed Mean Radiant Temperature (MRT) and UTCI in accordance with the theoretical framework of Di Napoli et al. (2020) and

ECMWF *thermofeel*. This approach accounts for solar geometry, solar-elevation-dependent projected area factors (f_p), and decomposed direct–diffuse solar fluxes alongside downwelling and upwelling terrestrial longwave radiation. By explicitly resolving these directional components rather than relying on uniform hemispheric simplifications, peak thermal load was moderated: no segments exceeded the extreme heat stress threshold (≥ 46ºC), demonstrating how refined radiative formulations recalibrate exposure estimates across complex topographies.

Finally, UTCI categories characterise a modelled thermal environment; they do not measure an individual cyclist's physiological strain or probability of heat-related illness. Périard et al. (2023) found that environmental indices, power output and physiological measures were associated in different ways during a professional multistage cycling race. Interpreting the present results as rider-level risk would require measurements of both the conditions experienced on the road and the responses of participating cyclists.

5.4 The vulnerable spectator: Static exposure in the roadside cauldron

A critical finding arising from the UTCI reconstruction concerns trackside spectators. While elite athletes possess exceptional cardiorespiratory capacity, heat-acclimatization status, and active support infrastructure (ice vests, cold-water bidons from team vehicles), the hundreds of thousands of roadside spectators have no such mitigation systems (Brocherie et al., 2015). The standard UTCI scale is directly calibrated to a pedestrian walking or standing at low metabolic rates. Therefore, while the UTCI serves as an atmospheric boundary proxy for riders, it directly measures the experiential thermal strain of stationary spectators. Along stages 4, 7, 8, and 9, fans remained static along unshaded asphalt roadsides for multiple hours awaiting the peloton during the hottest part of the afternoon. With localized UTCI values exceeding 38–44 °C, these microclimates expose crowds to acute risks (Matzarakis & Fröhlich, 2015). Elite sports sustainability must therefore broaden its scope from athlete-centric safety protocols to encompass public health surveillance along mobile routes.

5.5. The broadcasting of cycling competitions

From an environmental health perspective, scheduling stages earlier in the morning would eliminate most of the most severe heat-stress hours for both cyclists and crowds. However, professional road cycling operates within a commercial broadcasting model dominated by European television viewership and international broadcast rights (Solberg, 2002). Summer leisure patterns sharply reduce morning and late-evening television audiences, while the mid-to-late afternoon window (15:00–17:45 CEST) represents the primary viewership peak across major European broadcast networks. Organisers and commercial stakeholders deliberately schedule stage climaxes, such as mountain summit finishes and sprint finales, during this window to maximize live audience shares and advertising revenue. Consequently, as observed across other major international sports facing climate extremes (Orr et al., 2022), the timing of physical exertion is dictated by broadcasting economics rather than thermal biometeorology, subordinating athlete physiological safety and spectator well-being to media consumption schedules.

6. Conclusions

This study provides the first comprehensive spatial and temporal reconstruction of environmental heat stress along the 2026 Tour de France using high-resolution UTCI and WBGT modelling. The reconstructed profiles reveal substantial variation in environmental heat stress within and between stages of the 2026 Tour de France. In the preliminary analysis, approximately 87% of route distance and 86% of estimated riding time fell within strong, very strong or extreme UTCI heat stress categories. Comparing stages shows why both sustained conditions and local peaks matter: the stage with the highest mean UTCI was not the stage with the highest values.

No stage segment exceeded the UCI Extreme Weather Protocol's 32.2 °C WBGT threshold, although over 175 km fell within high-risk Red conditions (≥28 °C). This demonstrates that existing sports regulations should rely on dynamic and cumulative thermal heat stress.

Finalise these estimates after recalculating MRT and testing the sensitivity of UTCI categories to radiation assumptions and passage times. A valuable next step would be direct monitoring along the route, with calibrated temperature, humidity, wind and radiation sensors travelling with riders or support vehicles, complemented by stationary sensors at selected locations. Time-stamped mobile measurements could test how well the reconstructed profiles represent on-road conditions and help identify local effects the model does not resolve. Cvijanovic et al. (2026) likewise recommend mobile meteorological measurements alongside stationary observations for future Tour de France assessments.

References

Amaury Sport Organisation. (2026). *2026 route*. Tour de France. Retrieved September 18, 2026, from https://www.letour.fr/en/overall-route

Blocken, B., van Druenen, T., Toparlar, Y., Malizia, F., Mannion, P., Andrianne, T., Marchal, T., Maas, G. J., & van Hooff, T. (2018). Aerodynamic drag in cycling pelotons: New insights by CFD simulations and wind tunnel testing. Journal of Wind Engineering and Industrial Aerodynamics, 179, 319–337. 10.1016/j.jweia.2018.06.011

Boqué-Ciurana, A., Pozo, J. X. O., Sevil, J., & Saladié, Ò. (2025). Rescheduling summer human tower exhibitions? Thermal comfort increases in the evening. *Geographies*, *5*(3), 50**.**

Bouchama, A., Abuyassin, B., Lehe, C., Laitano, O., Jay, O., O'Connor, F. G., & Leon, L. R. (2022). Classic and exertional heatstroke. Nature Reviews Disease Primers, 8(1), 8. https://doi.org/10.1038/s41572-021-00334-6

Brocherie, F., Girard, O., & Millet, G. P. (2015). Emerging environmental challenges for outdoor elite sport events: Preparing for Tokyo 2020 and beyond. Scandinavian Journal of Medicine & Science in Sports, 25(S1), 3–6. https://doi.org/10.1136/bjsports-2024-108281

Bröde, P., Fiala, D., Błażejczyk, K., Holmér, I., Jendritzky, G., Kampmann, B., Tinz, B., & Havenith, G. (2012). Deriving the operational procedure for the Universal Thermal Climate Index (UTCI). *International Journal of Biometeorology, 56*, 481–494. https://doi.org/10.1007/s00484-011-0454-1

Cannon, A. J. (2018). Multivariate quantile mapping bias correction: an N-dimensional probability density function transform for climate model simulations of multiple variables. *Climate Dynamics*, 50(1-2), 31-49.

Cvijanovic, I., Begg, J. D., Mistry, M. N., Petrova, D., Brimicombe, C., & Sultan, B. (2026). The future of European outdoor summer sports through the lens of 50 years of the Tour de France. *Scientific Reports, 16*, Article 2644. https://doi.org/10.1038/s41598-025-30129-8

Erbs, D. G., Klein, S. A., & Duffie, J. A. (1982). Estimation of the diffuse radiation fraction for hourly, daily and monthly-average global radiation. *Solar Energy, 28*(4), 293–302. https://doi.org/10.1016/0038-092X(82)90302-4

Di Napoli, C., Barnard, C., Prudhomme, C., Cloke, H. L., & Pappenberger, F. (2021). ERA5-HEAT: A global gridded historical dataset of human thermal comfort indices from climate reanalysis. *Geoscience Data Journal, 8*, 2–10. https://doi.org/10.1002/gdj3.102

Di Napoli, C., Hogan, R. J., & Pappenberger, F. (2020). Mean radiant temperature from global-scale numerical weather prediction models. *International Journal of Biometeorology, 64*, 1233–1245. https://doi.org/10.1007/s00484-020-01900-5

Hersbach, H., Bell, B., Berrisford, P., Hirahara, S., Horányi, A., Muñoz-Sabater, J., Nicolas, J., Peubey, C., Radu, R., Schepers, D., Simmons, A., Soci, C., Abdalla, S., Abellan, X., Balsamo, G., Bechtold, P., Biavati, G., Bidlot, J., Bonavita, M., ... Thépaut, J.-N. (2020). The ERA5 global reanalysis. *Quarterly Journal of the Royal Meteorological Society, 146*, 1999–2049. https://doi.org/10.1002/qj.3803

Holthuijzen, M. F., Beckage, B., Clemins, P. J., Higdon, D., & Winter, J. M. (2021). Constructing high-resolution, bias-corrected climate products: A comparison of methods. *Journal of Applied Meteorology and Climatology, 60*(4), 455–475. https://doi.org/10.1175/JAMC-D-20-0252.1

Intergovernmental Panel on Climate Change. (2021). Chapter 12: Climate change information for regional impact and for risk assessment. In *Climate change 2021: The physical science basis*. https://www.ipcc.ch/report/ar6/wg1/chapter/chapter-12/

Matzarakis, A., & Fröhlich, D. (2015). Sport events and climate for visitors—The case of FIFA World Cup in Qatar 2022. International Journal of Biometeorology, 59(4), 481–486. https://doi.org/10.1007/s00484-014-0886-5

Météo-France. (2026). *Données climatologiques de base – horaires* [Data set]. https://www.data.gouv.fr/datasets/donnees-climatologiques-de-base-horaires

Mues, A., Lauer, A., Lupascu, A., Rupakheti, M., Kuik, F., & Lawrence, M. G. (2018). WRF and WRF-Chem v3.5.1 simulations of meteorology and black carbon concentrations in the Kathmandu Valley. *Geoscientific Model Development, 11*, 2067–2091. https://doi.org/10.5194/gmd-11-2067-2018

National Centre for Atmospheric Research. (n.d.). *The WRF Preprocessing System (WPS).* https://www2.mmm.ucar.edu/wrf/users/wrf_users_guide/build/html/wps.html

Natural Earth. (n.d.). *Natural Earth* [Map data]. https://www.naturalearthdata.com/

Obradovich, N., & Fowler, J. H. (2017). Climate change may alter human physical activity patterns. *Nature Human Behaviour, 1*, Article 0097. https://doi.org/10.1038/s41562-017-0097

Olano Pozo, J. X., Saladié, Ò., & Boqué-Ciurana, A. (2024). Rising temperatures, wavering human towers? Temperature trends and thermal comfort during castells exhibitions in Catalonia (1951–2023): Case studies in Valls (24 June), La Bisbal del Penedès (15 August), Tarragona (19 August), and Vilafranca del Penedès (30 August). *Climate, 12*(8), Article 112. https://doi.org/10.3390/cli12080112

Olano Pozo, J. X., Boqué-Ciurana, A., & Saladié, Ò. (2026). Under the Heat of Tradition: Thermal Comfort During Summer Correfocs in Catalonia (1950–2023). *Climate*, *14*(1), 15.

Orr, M., Inoue, Y., Seymour, R., & Dingle, G. (2022). Impacts of climate change on organized sport: A scoping review. WIREs Climate Change, 13(3), e760. https://doi.org/10.1002/wcc.760

Périard, J. D., Wilson, M. G., Tebeck, S. T., Gilmore, J. B., Stanley, J., & Girard, O. (2023). Influence of the thermal environment on work rate and physiological strain during a UCI World Tour multistage cycling race. *Medicine & Science in Sports & Exercise, 55*(1), 32–45. https://doi.org/10.1249/MSS.0000000000003028

Racinais S, Hosokawa Y, Akama T, et al. (2023). IOC consensus statement on recommendations and regulations for sport events in the heat.). British Journal of Sports Medicine, 57, 8–25. https://doi.org/10.1136/bjsports-2022-105942

Racinais, S., Alonso, J. M., Coutts, A. J., Flouris, A. D., Girard, O., González-Alonso, J., Hausswirth, C., Jay, O., Lee, J. K., Mitchell, N., Nassis, G. P., Nybo, L., Pluim, B. M., Roelands, B., Sawka, M. N., Wingo, J., & Périard, J. D. (2015). Consensus recommendations on training and competing in the heat. British Journal of Sports Medicine, 49(18), 1164–1173. https://doi.org/10.1136/bjsports-2015-094915

Saladié, Ò., Boqué-Ciurana, A., Sevil, J., & Olano Pozo, J. X. (2025). Summer thermal comfort in urban squares: The case of human tower exhibitions in Catalonia. *Atmosphere*, *16*(6), 666.

Servei Meteorològic de Catalunya (SMC). (n.d.). *Dades meteorològiques de la XEMA* [Data set]. Dades obertes de Catalunya. https://analisi.transparenciacatalunya.cat/Medi-Ambient/Dades-meteorol-giques-de-la-XEMA/nzvn-apee (accessed 1 October 2026).

Skamarock, W. C., Klemp, J. B., Dudhia, J., Gill, D. O., Liu, Z., Berner, J., Wang, W., Powers, J. G., Duda, M. G., Barker, D. M., & Huang, X.-Y. (2019). *A description of the Advanced Research WRF Model version 4* (NCAR Technical Note NCAR/TN-556+STR). National Centre for Atmospheric Research. https://doi.org/10.5065/1dfh-6p97

Solberg, H. A. (2002). The economics of television sports rights: Europe and the USA. European Sport Management Quarterly, 2(4), 281–298. https://doi.org/10.1080/1029712x.2000.12426513

Tartarini, F., & Schiavon, S. (2020). pythermalcomfort: A Python package for thermal comfort research. *SoftwareX, 12*, Article 100578. https://doi.org/10.1016/j.softx.2020.100578

Valenzuela, P. L., Mateo-March, M., Zabala, M., Muriel, X., Lucia, A., Barranco-Gil, D., & Pallarés, J. G. (2022). Ambient temperature and field-based cycling performance: Insights from male and female professional cyclists. *International Journal of Sports Physiology and Performance, 17*(7), 1025–1029. https://doi.org/10.1123/ijspp.2021-0508